Characteristics of hydraulic conductivity in mountain block systems and its effects on mountain block recharge: Insights from field investigation and numerical modeling

Yunmei Fu, Yanhui Dong, Liheng Wang, Olivier Bour, Maria V Klepikova, Zihua Zong, Zhifang Xu, Zhichao Zhou

Journal Pre-proofs

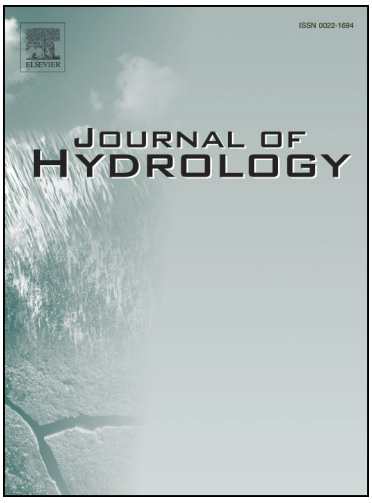

Research papers

Characteristics of hydraulic conductivity in mountain block systems and its effects on mountain block recharge: Insights from field investigation and numerical modeling

Yunmei Fu, Yanhui Dong, Liheng Wang, Olivier Bour, Maria V. Klepikova, Zihua Zong, Zhifang Xu, Zhichao Zhou

PII: S0022-1694(22)00757-0
DOI: https://doi.org/10.1016/j.jhydrol.2022.128184
Reference: HYDROL 128184

To appear in: *Journal of Hydrology*

Received Date: 26 January 2022
Revised Date: 3 July 2022
Accepted Date: 5 July 2022

Please cite this article as: Fu, Y., Dong, Y., Wang, L., Bour, O., Klepikova, M.V., Zong, Z., Xu, Z., Zhou, Z., Characteristics of hydraulic conductivity in mountain block systems and its effects on mountain block recharge: Insights from field investigation and numerical modeling, *Journal of Hydrology* (2022), doi: https://doi.org/10.1016/j.jhydrol.2022.128184

Characteristics of hydraulic conductivity in mountain block systems and its effects on mountain block recharge: Insights from field investigation and numerical modeling

Yunmei Fu[a,b,c], Yanhui Dong[a,b,c,*], Liheng Wang [a,b,c], Olivier Bour[d], Maria V. Klepikova[d], Zihua Zong[e,f], Zhifang Xu[a,b,c], Zhichao Zhou[e,f]

[a] Key laboratory of Shale Gas and Geoengineering, Institute of Geology and Geophysics, Chinese Academy of Sciences, Beijing 100029, China

[b] Innovation Academy for Earth Science, Chinese Academy of Science, Beijing 100029, China

[c] College of Earth and Planetary Science, University of Chinese Academy of Sciences, Beijing 100049, China

[d] Univ Rennes, CNRS, Géosciences Rennes, UMR 6118, 35000 Rennes, France

[e] Beijing Research Institute of Uranium Geology, Beijing 100029, China

HLW: High-level radioactive waste; MBR: Mountain block recharge; MFR: Mountain-front recharge; STEP: Scientific Expedition and Research Program; TDS: Total dissolved solid; URL: Underground research laboratory; IQR: interquartile range

[f] CAEA Innovation Center for Geological Disposal of High-level Radioactive Waste, Beijing 100029, China

*Corresponding Author;

Yanhui Dong

Key laboratory of Shale Gas and Geoengineering, Institute of Geology and Geophysics, Chinese Academy of Sciences, Beijing 100029, China

Phone: +86 13910954926

Fax: +86 10 82998617

Email: dongyh@mail.iggcas.ac.cn

Abstract

The process wherein groundwater flowing from mountain bedrock into lowland and adjacent alluvial aquifers, known as mountain-block recharge (MBR), is found across various climatic and geological settings. An understanding of the potential groundwater flow paths in mountain block systems is necessary for comprehending MBR spatial distribution. However, poorly characterized mountain block hydraulic properties, and especially a lack of direct measurements of hydraulic conductivity (K) at depths >200

m, limit the characterization and quantifications of the MBR processes. In this study, we analyze hydraulic data set, namely 555 in-situ *K* measurements at various depths from two borehole sections extending from mountain block to mountain front in a potential disposal site for high-level radioactive waste. The *K* dataset was categorized into two groups: one for bedrock and another for fault zones, which was further classified into fault core *K*, damage zone *K*, and general fault zone *K*. Using a permeability conceptual model and multiple scenarios numerical modelling, this study examined the potential flow paths of MBR processes, mainly focusing on the characteristics of *K* in bedrocks and the hydraulic role of fault zones in mountain block systems. The distribution of Bedrock *K* supports the assumption of decreased trend with depth. A logarithmic fit through Bedrock *K* and depth pairs resulted in Log(K) = -1.62*Log(z) - 6.52, with low predictive power. This study illustrated the localized effects and spatially variable roles of fault zones in MBR within this particular hydrogeological configuration in Beishan, China. Our results provide insights into the MBR process in crystalline mountain block systems. Additionally, the hydraulic conductivity presented here provides data on the subsurface properties of mountain block systems in a crystalline area, and further facilitates the characterization and quantification of mountain-block recharge.

Keywords: mountain block recharge, mountain hydrogeology, fractured aquifer

1 Introduction

Mountainous areas play an important role in the global water cycle and constitute the water source for numerous populated regions at lower elevations (Jódar et al., 2017; Lone et al., 2021; Somers and McKenzie, 2020; Viviroli et al., 2020; Wilson and Guan, 2004). Water from mountainous areas recharges lowlands via mountain-front recharge (MFR) and mountain-block recharge (MBR; (Aishlin and McNamara, 2011; Ajami et al., 2011; Bresciani et al., 2018; Manning and Solomon, 2003; Markovich et al., 2019; Peng et al., 2018; Taucare et al., 2020; Wilson and Guan, 2004). MFR refers to the focused and net infiltration from perennial and ephemeral streams originating in the mountain block, which occurs at the piedmont zone (Markovich et al., 2019; Wilson and Guan, 2004). MBR refers to the groundwater flow from the mountain block into an adjacent alluvial aquifer, and is also referred to as "inter-aquifer recharge" (Healy, 2010) or "subsurface inflow" (Manning and Solomon, 2003). MBR may recharge adjacent aquifers by two processes: diffuse MBR and focused MBR (Wilson and Guan, 2004). Diffuse MBR occurs widely within mountain blocks, including the mountain front area (Markovich et al., 2019; Wilson and Guan, 2004). Focused MBR corresponds to groundwater flow through permeable colluvium-alluvium corridors in gullies or canyons joining the adjacent basin, and oblique basement faults crossing the mountain

front area, which may promote groundwater flow into the adjacent basin (Figueroa et al., 2021; Markovich et al., 2019; Wilson and Guan, 2004).

Previous studies have largely focused on understanding the fundamental factors determining the location and extent of MBR, with the hydraulic conductivity (K) distribution within mountain bedrock and the role that fault zones play being two vital factors (Gleeson and Manning, 2008; Markovich et al., 2019; Welch et al., 2012; Wilson and Guan, 2004). K distribution was identified as one of the first-order controls of the rate and distribution of MBR (Forster and Smith, 1988; Gleeson and Manning, 2008; Haitjema and Mitchell-Bruker, 2005; Markovich et al., 2019; Welch et al., 2012; Wilson and Guan, 2004). The general conceptual model for mountain groundwater flow systems is composed of a higher-K "active" zone (the aquifer) that overlies a deep low-K zone (relatively impermeable bedrock) (Manning and Caine, 2007; Markovich et al., 2019; Welch et al., 2012). The existence of an "active" zone with $K > 10^{-8}$ m^{-1} where active mountain groundwater flow can be produced, and a recharge rate greater than roughly 10 mm/year are prerequisites for the occurrence of MBR (Markovich et al., 2019). If some MBR exists, major faults near the mountain front can potentially either impede or enhance MBR. Theoretically, major faults oriented at a high angle to the MBR flow paths might act as barriers to MBR as the groundwater must flow across the fault zone to enter the adjacent aquifers (Chowdhury et al., 2008; Delinom, 2009;

Figueroa et al., 2021; Kebede et al., 2008). In contrast, obliquely oriented faults (more parallel to MBR flow paths) within the bedrock could act as conduits for groundwater flow and promote MBR (Figueroa et al., 2021). However, the results from field examination, hydrochemical, and groundwater age assessment provide evidence that the orientations of faults do not determine their role in mountain block hydrogeological processes (Caine et al., 2017; Kebede et al., 2008), and the oblique oriented faults could act as barriers to MBR. Therefore, the possible permeability structure and the actual hydraulic influence of mountain-block faults in MBR processes (impeding or enhancing) remain speculative.

Although the vital controls of the MBR process have been identified, the characterization and quantification of MBR processes remain challenging in mountain block hydrogeology because of the intrinsic heterogeneity of *K* distribution and fault zones and data limitation, particularly of subsurface data from the mountain block and mountain front (Markovich et al., 2019; Yao et al., 2017).

Several studies proposed to bypass determining actual *K* distribution by employing synthetic or semi-synthetic subsurface *K* structures in models (Engdahl and Maxwell, 2015; Gleeson and Manning, 2008; Voeckler et al., 2014; Wang et al., 2018a; Welch et al., 2012). Few studies are based on the actual *K*, using data sets at depths of 0–20 m (Ameli et al., 2018) and 10–200 m (Welch and Allen, 2014). Most of these works have

106 generally converged that the typical groundwater active circulation depth for fractured
107 crystalline rock environments may extend to 200 m subsurface, with $K = 10^{-8}$ m·s^{-1}
108 (Manning and Ingebritsen, 1999; Markovich et al., 2019; Rapp et al., 2020), surpassing
109 the *K* data depth previously used. In addition, the target depth of geo-environmental
110 systems engineering related to mountain groundwater systems is much deeper. For
111 example, the site selection for long-term nuclear waste is targeted at 300–500 m (Tóth
112 and Sheng, 1996; Voss and Provost, 2001; Wang et al., 2018b); whereas CO_2 geological
113 storage target depths are $\geq$ 800 m (Bickle, 2009; Gunter et al., 2004). In contrast, direct
114 subsurface measurements of *K* at depths > 200 m are rare (Markovich et al., 2019).
115 Therefore, studies providing access to a range of actual bedrock properties (especially
116 K) at depths > 200 m should be prioritized in mountain block system hydrogeology.

117 In this study, we report a series of in-situ measured hydraulic conductivities (n = 555)
118 from a crystalline mountain block system to complement hydrogeological databases at
119 depths >200 m in mountain systems. The data set includes *K* measured in crystalline
120 bedrock (n = 512) and within fault zones (n = 43), ranging from 0 m to 592.3 m below
121 the ground surface (mbgs). All data were obtained from the Beishan area, Gansu
122 Province, China, a disposal site for high-level radioactive waste (HLW). Given the
123 possibility of groundwater acting as a carrier of radionuclides, understanding the flow
124 paths in MBR processes in the study area is critical for determining the safety of HLW

125 disposal. Based on a permeability conceptual model and numerical modelling built on
126 in-situ measurements, this study explores the possible flow paths for MBR in this area,
127 focusing on the *K* distribution, associated heterogeneity and the hydraulic role of fault
128 zones.

129 **2 Study area**

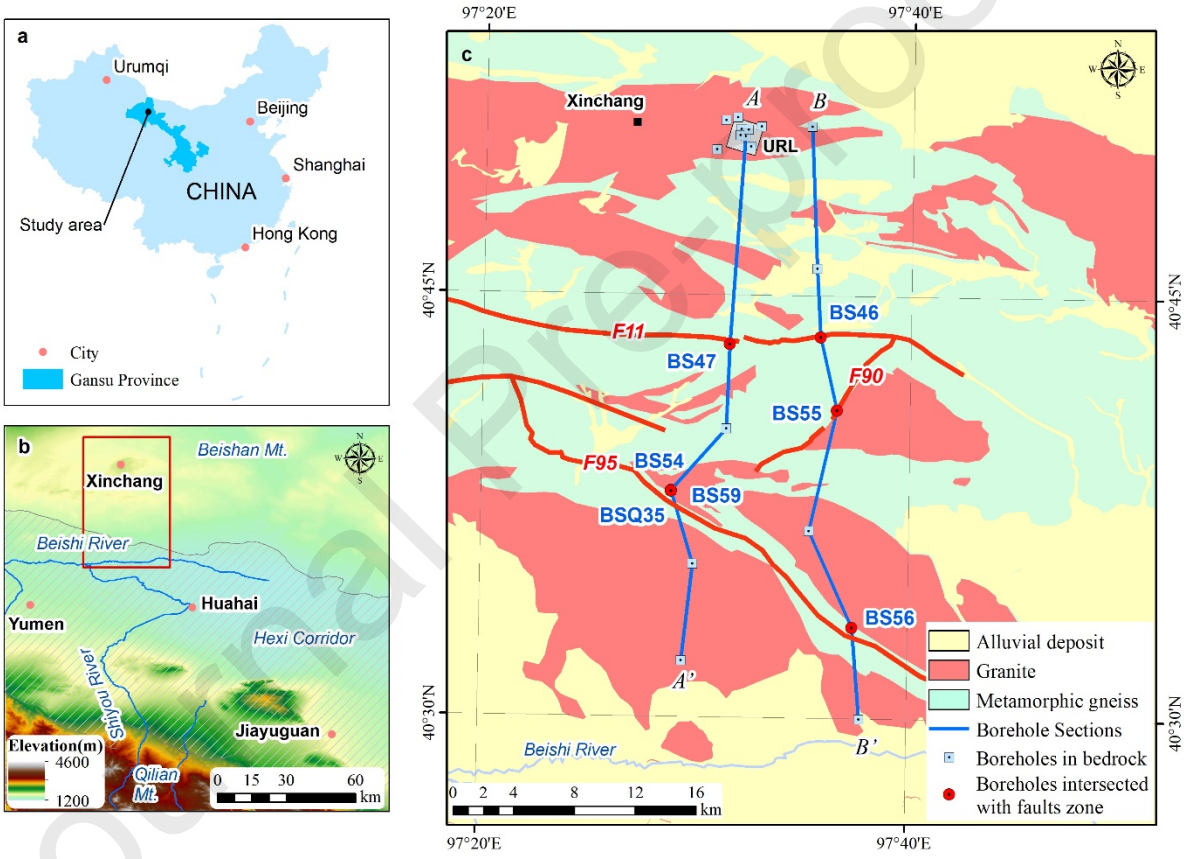

130

Figure 1. a. Location of the study area, b. topography of the study area, and c. borehole sections (where field data were obtained) and geology.

131 This study was conducted in the Beishan area situated in the Gansu Province of

132 northwestern China (Fig 1a). The study area is an inland mountain range covering an
133 area of approximately 3,973.9 km^2 and is located north of the Huahai Basin in the Hexi
134 Corridor, where multiple cities (including Yumen, Jiayuguan, and Huahai) with more
135 than 9 million inhabitants are located. With an altitude ranging between 873 m and
136 2,556 m above sea level, the Beishan area primarily consists of low altitude mountains
137 and small hills. The Xinchang Site, which is the prospective location for China's HLW
138 repository and the location of China's first underground research laboratory (URL), is
139 located to the southwest of the Beishan area and is approximately 60 km from the
140 nearest city of Yumen (Fig 1b). The site covers an area of >100 km^2 with an altitude
141 ranging between 1,400 and 1,800 m (Zhou et al., 2020)

142 Metamorphic rocks (mainly Ordovician or Silurian gneiss), intrusive rocks (mainly
143 Permian granite) and sediments (mainly Quaternary clay and sandy loam weathered
144 from gneiss and granite) comprise the main lithology of the study area, with occasional
145 alluvium deposits (usually <10 m) in the ground (Peng, 2013; Wang et al., 2018b). The
146 cores obtained from the Xinchang Site are dominated by gneissic biotite monzonitic
147 granite and biotite granodiorite (Zhao et al., 2016).

148 The Beishan area is characterized by an arid climate with an annual average
149 precipitation of 73.1 $mm \cdot yr^{-1}$ and a mean annual potential evaporation of >3,000 mm
150 (Zhou et al., 2020). Except for the Beishi River, a river originating from Qilian

151 Mountain and flows eastward passing the study area, no other perennial river is found
152 within the area due to extreme drought, although ephemeral deluge can occur after brief
153 precipitation events in the summer (Cao et al., 2017a; Cao et al., 2017b; Dong et al.,
154 2009).

155

156 Several faults have been identified in the study area, including two major faults (F11
157 and F95), and several local faults (F90). The fault kinematics and architectures, as
158 determined by surface geological mapping and borehole drilling, are provided in Table
159 1 (Gansu Geology Survey, 1978; Guo et al., 2003; Guo et al., 2014; Wang et al., 2018b).
160 The F11 fault is located in a metamorphic gneiss south of the Xinchang Site and is
161 approximately perpendicular to the mountain slope. F90 is the most representative of
162 the secondary faults of F11 and is located in granite and metamorphic gneiss (Gansu
163 Geology Survey, 1978). The F95 fault is an NW striking fault developed in
164 metamorphic gneiss between two intrusive granite zones and extends directly from the
165 mountain front to the Huahai Basin (Gansu Geology Survey, 1978; Guo et al., 2003;
166 Guo et al., 2014; Wang et al., 2018b).

Table 1. Fault kinematics and architectures.

Section	Fault	Strike	Dip	Geology	Thickness

					Total zone (m)	Fault core (m)	Damage zone (m)
A-A’	F11	W-SW	70	Metamorphic gneiss	-	10.6	-
	F95	NW-SE	78	Metamorphic gneiss	64.4	30.2	34.2
B-B’	F11	W-SW	60	Metamorphic gneiss	-	1.4	-
	F90	NE-SW	60	Granite & Metamorphic gneiss	52.4	-	-
	F95	NW-SE	75	Metamorphic gneiss	67.0	1.6	65.4

Hydrogeochemical characteristics reveal the evolution processes of groundwater by recording the interaction between groundwater and the aquifer medium. Accordingly, the hydrogeochemical data of groundwater in the Beishan area were comprehensively collected from published literature, revealing a range of pH values from 7.39 to 10.14, groundwater temperature between 8 and 17 °C, and a total dissolved solid (TDS) content of 0.7–19.0 $g \cdot L^{-1}$ (Guo et al., 2014; Li, 2020; Wang et al., 2018b; Wang, 2015). In particular, high TDS was observed in shallow groundwater, indicating that the

174 groundwater underwent strong evaporation. Based on isotopic data and groundwater
175 age, previous studies have also shown that groundwater in the study area is recharged
176 primarily by local precipitation (Li, 2020). The groundwater flow is controlled by
177 topography (Dong et al., 2009; Wang, 2015).

178 **3. Methods**

179 *3.1 Hydraulic conductivity measurements, categories, and characterization*

180 3.1.1 *K* measurements and categories

181 A total of 555 hydraulic conductivity measurements were obtained from 22 boreholes
182 (Table 1). Boreholes were drilled through the surface weathering rock and into the
183 bedrock, reaching a maximum depth of 690.7 m, permitting the characterization of the
184 mountain block hydraulic conductivity. All data were obtained via in-situ tests
185 (including constant-head injection, plug, or slug tests using packer systems); therefore,
186 these data are all defined as bulk permeability instead of matrix permeability (Scibek,
187 2020; Scibek et al., 2016). The measuring intervals of in-situ tests differ from 12 to 50
188 m along the boreholes, and were also extended to 202 m to investigate the fault zones
189 intersected by the boreholes.

190 Seven of the 22 boreholes have intersected fault zones. Data from all 555 hydraulic

191 conductivity measurements were classified into two categories based on the measured
192 locations: Bedrock *K*, which refers to *K* obtained from in-situ tests conducted away
193 from any fault zones (n = 512, shown as blue squares in Figure 2), and *K* measured in
194 fault zones (n = 43, shown as circles in Figure 2). For *K* measured in fault zones, the
195 data were further divided into three categories: Core zone *K*, which refers to the data
196 obtained within the zone that is clearly identified as a fault core and isolated in the in-
197 situ tests (n = 2, shown as yellow circles in Figure 2); Damage zone *K,* which refers to
198 the data measured only within the fault damage zone (n = 33, shown as red circles in
199 Figure 2); and General fault *K*, which refers to the data from test intervals including
200 both fault damage zones and the main fault core zones (n = 8, shown as green circles in
201 Figure 2). General fault *K* occurred due to either of two reasons: the isolation of the
202 fault core zone or damage zone was not available for in-situ tests due to potential
203 collapsibility of boreholes, or, it was difficult to clearly identify the damage and fault
204 core zones within a fault zone.

205 The Bedrock *K* data (n = 512, shown as blue squares in Figure 2a) was divided into
206 measurement depth intervals of 50 m, and the arithmetic mean, median, 10% and 90%
207 confidence distribution of each interval were calculated. A linear regression of log
208 hydraulic conductivity (log *K*) over log depth (log *z*) was performed on the Bedrock *K*
209 data, considering the previous understanding that *K* decays exponentially with an

increase in depth (Achtziger-Zupančič et al., 2017).

3.1.2 Characterization of permeability structure

A vertical layer profile of the study area was created based on the data. Instead of adapting detailed definitions and descriptions of weathering and fracture, the vertical distribution of K and its relative differences established the primary principles for constructing a conceptualized model of the mountain block systems.

From a hydrogeological perspective, a domain can be viewed as a pervious formation with $K \geq$ 1.00 E-8 m·s^{-1}, where active groundwater flow may be produced (Katsura et al., 2009; Markovich et al., 2019; Welch and Allen, 2014). Therefore, a threshold value of K_0 = 1.00 E-8 m·s^{-1} was adapted to indicating K's relative difference by depth in bedrock. The probability $K > K_0$ (P) and the arithmetic mean K value of every 50 m depth were calculated. Based on the calculated results and the vertical conceptual model for fractured crystalline-rock mountain block system of Welch and Allen (2014), the vertical permeability structure of the mountain block in the study area was then divided into three layers: the Weathered Zone (including soil and highly weathered rock), the Fractured Zone, and the Inactive Zone (relatively impermeable bedrock with majority of $K < K_0$, where active groundwater may not be produced).

The permeability ratios (Scibek, 2020) can be used to quantify the "conduit" or "barrier"

magnitudes of a fault zone using the permeability of the general fault zone (or fault core) and host rock obtained at specific locations (ideally along the same drillhole or outcrop section). In this study, permeability (m^2) was replaced with hydraulic conductivity ($m \cdot s^{-1}$) in the calculation for data consistency, and therefore refers to this ratio as hydraulic conductivity ratio (*K* ratio).

$$K\ ratio = log_{10}\frac{K_{General\ fault\ zone/\ Core}}{K_{Host\ rock}}$$

3.2 Groundwater flow analysis– numerical modelling

To investigate the flow behavior of faults in the study area, a 2D hydrogeological numerical model coupled with particle tracking was applied. MODFLOW-USG was used to simulate the hydrogeological processes of mountain blocks, and Darcy's Law Module was used to describe groundwater flow. We constrained the model based on the topographical section B-B', as well as the hydraulic properties described in Section 4.

4. Results

4.1 Characteristics of hydraulic conductivity

4.1.1 Hydraulic conductivity of bedrock

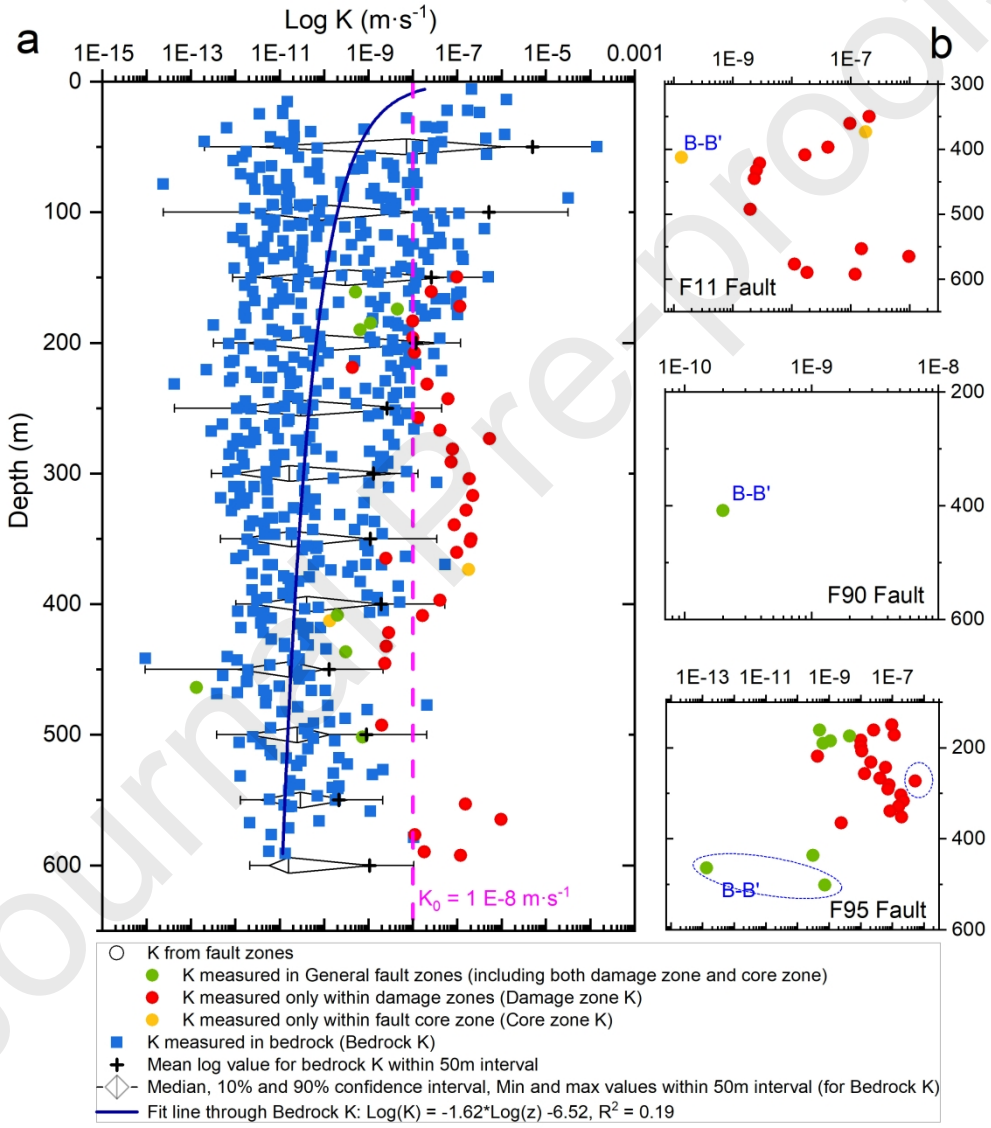

Figure 2. Distribution of hydraulic conductivity (K) with depth, a. Depth trend of K for bedrock (n = 512, shown as blue squares) and fault zones (n = 43, shown as circles) derived from in-situ hydraulic testing in 22 boreholes; b. K from three faults, i.e., F11 fault, F90 fault and F95 fault.

Figure 2a shows *K* distribution with depth in the study area, including Bedrock *K* (n = 512) and *K* from fault zones (n = 43). Both the highest hydraulic conductivity (1.40 E-4 $m \cdot s^{-1}$ at 50.0 m depth) and lowest hydraulic conductivity (9.39 E-15 $m \cdot s^{-1}$ at 441.5 m depth) were observed in Bedrock *K*. Only two of the 555 *K* data are greater than 1.00 E-5 $m \cdot s^{-1}$, both within the depth less than 100.0 m. The hydraulic conductivity data is shown to be more scattered at shallow depths than at deeper ones, and shows substantial variance near the surface.

A logarithmic fit through Bedrock *K* and depth pairs resulted in $Log(K) = -1.62 * Log(z) - 6.52$, with low predictive power ($R^2 = 0.19$). The slope of the regression reveals that the hydraulic conductivity averages 1.62 orders of magnitude per order of magnitude of depth change.

4.1.2 Fault zone hydraulic conductivity

Figure 2b shows 43 *K* measured in fault zones (2 Core zone *K*, 33 Damage zone *K*, and 8 General fault zone *K*), revealing the permeability of three faults: F90, F95 and F11.

For F11, two Core zone K were measured in boreholes at different locations that showed a large variance: 1.80 E-7 $m \cdot s^{-1}$ in the western part (A-A'), and 1.34 E-10 $m \cdot s^{-1}$ in the eastern part (B-B'). All Damage zone K of F11 were obtained from the same borehole located in the western part (A-A') and are distributed within 2 orders of magnitudes (1.97 E-9 $m \cdot s^{-1}$ – 9.71 E-7 $m \cdot s^{-1}$).

The overall hydraulic conductivity of F90 (including fault core and damage zone) was low permeable with a General fault zone K of 2.00 E-10 $m \cdot s^{-1}$. For F95, General fault zone K obtained from the western part (B-B') ranged from 1.33 E-13 $m \cdot s^{-1}$ to 7.31 E-10 $m \cdot s^{-1}$, with the ones from the western part (A-A') showing a larger variance. Damage zone K were all centralized between 4.31 E-10 $m \cdot s^{-1}$ and 5.35 E-7 $m \cdot s^{-1}$.

4.2 Mountain-basin conceptual model

4.2.1 Bedrock permeability structure

Based on the calculated results and the vertical conceptual model for fractured crystalline-rock mountain block system of Welch and Allen (2014), the vertical permeability structure of the mountain block in the study area can be classified into three layers: 0–50 mbgs for the Weathered Zone (including soil and highly weathered rock), 50–350 mbgs for the Fractured Zone, and >350 mbgs for the Inactive Zone (relatively impermeable bedrock with majority of $K < K_0$).

277 The arithmetic mean value of K was 4.80 E-6 $m \cdot s^{-1}$, 1.01 E-7 $m \cdot s^{-1}$, and 9.08 E-10 $m \cdot s^{-1}$
278 for the Weathered Zone, Fractured Zone, and Inactive Zone respectively. The
279 proportion of $K \geq K_0$ was 48.28% within the Weathered Zone, whereas it decreased to
280 13.22% within the Fractured zone and to 2.24% within the Inactive Zone (350–600 m).

281 To better reveal the hydraulic properties of each layer, the interquartile range (IQR)
282 measure of statistical dispersion was used to remove extreme K values in each layer.
283 Subsequently, the arithmetic mean K values of the three layers were recalculated as
284 1.16 E-8 $m \cdot s^{-1}$ for the Weathered Zone, 5.69 E-9 $m \cdot s^{-1}$ for the Fractured Zone, and 9.08
285 E-10 $m \cdot s^{-1}$ for the Inactive Zone.

286 4.2.2 Permeability structure of faults

287 Table 3 lists the calculated K ratios of faults, indicating their potential permeability
288 structures in the study area. The K ratio of F11 in the western part (A-A') was 2.64,
289 which indicates a potential conduit for groundwater; however, the ratio in the eastern
290 part (B-B') was -1.81, which suggests a potential barrier for groundwater. This
291 inconsistency in hydraulic properties implies possible spatial variability in permeability
292 structure for the same fault.

293 In contrast to F11, F95 shows consistency in K ratios: -0.75 and -0.53 for the western
294 part (A-A') and the eastern part (B-B') respectively, indicating that F95 may impede

295 groundwater flow and acts as a "barrier". *K* ratio of -0.96 for F90 also suggests a
296 potential "barrier" for groundwater flow.

*Table 2 Fault information and calculated K ratios (*represented averaged values)*

Section	Fault	General fault zone K	Core zone K	Host rock K	K ratio
A-A'	F11	-	3.00E-7	4.15E-10*	2.86
	F95	1.41E-9*	-	7.89E-9*	-0.75
B-B'	F11	-	1.34E-10	8.74E-9*	-1.81
	F90	2.00E-10	-	1.84E-9*	-0.96
	F95	3.68E-10*	-	1.25E-9*	-0.53

297 4.2.3 Conceptual model

298 A conceptual hydrogeological model of the study area is shown in Figure 3. Based on
299 the permeability structures of bedrock and faults, the 2D conceptual model was
300 vertically divided into three layers. The arithmetic mean *K* values with extreme values
301 removed by the interquartile range (IQR) method were selected to represent each zone.
302 Three faults (F11, F90, and F95) were considered in this conceptual model. The
303 hydraulic conductivity of F95 and F90 were labelled according to the information
304 obtained on the eastern part (B-B'). However, their hydraulic impact remains the
305 primary source of uncertainty in this conceptual model for characterizing groundwater
306 flow patterns in the study area.

307

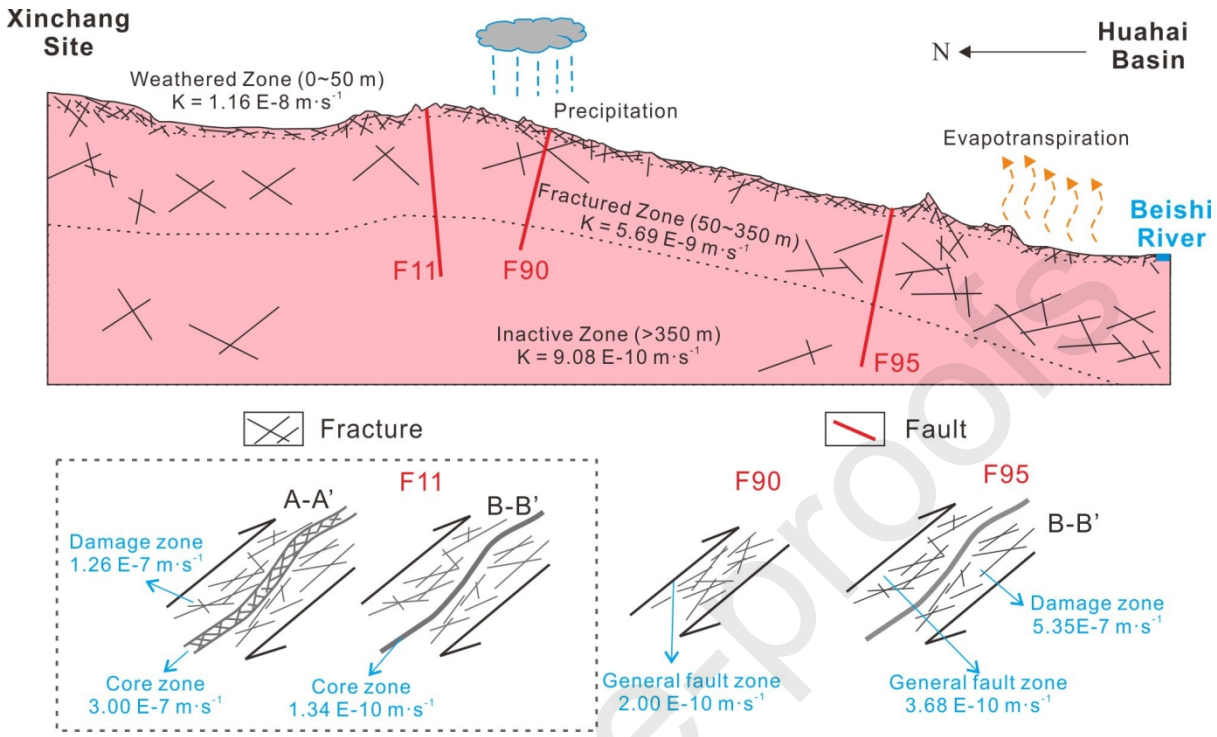

308

Fig 3. Conceptual hydrogeological model of the study area, and the permeability structures of faults (A-A', B-B' representing the sections where hydraulic conductivity was measured).

309 *4.3 Groundwater flow patterns in study area – numerical model results*

310 4.3.1 Model scenarios and setup

311 The following four field scenarios were developed based on the permeability
312 conceptual model built in Section 4.2: homogeneous permeability, layered permeability,
313 layered permeability with low permeable core zone of F11, and layered permeability

314 with high permeable core zone of F11. All scenarios were simulated in steady state flow,
315 with Scenarios 3 and 4 designed to investigate the potential hydrogeological role of F11,
316 F90, and F95 faults. The scenario details are as follows:

317 *Homogeneous* scenario: Served as the baseline model, where an arithmetic mean *K*
318 value of the weathered zone calculated in Section 4.1 (1.16 E-8 $m \cdot s^{-1}$) was applied
319 to represent the general hydraulic conductivity. This approach maintained a
320 constant hydraulic property of the model domain, allowing the results to reflect a
321 direct control of topography on groundwater flow patterns within the study area.
322 *Layered: without faults* (Layered permeability field) scenario: Here, the
323 permeability was consistent with the conceptual model in Section 4.2.3, except for
324 the faults. This scenario did not include faults, an appropriate assumption when
325 controlling for the vertical distribution of *K* along the hydrogeological conditions
326 of mountain blocks.
327 *Layered: low K fault* (Layered permeability field scenario with low permeable core
328 zone of F11) scenario: Building upon the former scenario, but considering three
329 faults (F11, F90, and F95). F11 and F95 were conceptualized as damage zones and
330 fault cores. The measurements of the western part (B-B') of F95 were used to
331 represent this fault: an average of General Fault zones *K* (3.68 E-10 $m \cdot s^{-1}$) was
332 assigned to the core zone (as no measurement was available within the F95 fault

core); the measured Damage zone *K* (5.35 E-7 $m \cdot s^{-1}$) was used for damage zone. For F11, the lower measured value of 1.34 E-10 $m \cdot s^{-1}$ was selected to represent the permeability of F11 fault core (Figure 3), and the damage zone hydraulic conductivity was 1.26 E-7 $m \cdot s^{-1}$.

Layered: high K fault (Layered permeability field with a highly permeable core zone of F11) scenario: Building upon the former scenario, but replacing the *K* value of F11 fault core zone with 3.00 E-7 $m \cdot s^{-1}$.

The upper boundary of this model was conceptualized as a constant-head boundary to reflect the high correlation between hydraulic head and topography within the study area. At this boundary point, the groundwater head was identical to the ground elevation. The Beishi River, located at the foot of the mountain bedrock, was also regarded as a constant-head boundary; whereas the lateral and lower boundaries were specified as no-flow boundaries. Precipitation and evaporation were not considered in the model. While the study area has a typical arid climate (low precipitation, high evaporation), this assumption is appropriate as the model simulates the general topography and hydraulic properties of groundwater flow patterns under steady state flow. This approach allows for a clearer understanding of the groundwater flow pattern response to change in hydraulic properties (e.g., fault zones).

The model domain was divided into 39,056 unstructured grids, and the meshes were

352 required to be finer around the model boundaries and faults. Meshing quality was
353 examined to ensure that each fault zone contained multiple elements was fully
354 described in the model. Particle tracking was employed to investigate the differences in
355 groundwater flow paths between model scenarios. A total of 2,038 particles were set
356 up along the ground boundary, and their traces were recorded and exported.

357 4.3.2 Model results

358 Simulation results for the four scenarios are shown in Figure 4, where multiple types of
359 streamlines distributions are presented (only representative streamlines were showed
360 for distinguishability). Multiple types of streamlines (A, B, C, and D) are labelled to
361 illustrate the differences in groundwater flow patterns: A represents the streamlines
362 reaching deep positions; B represents the streamlines at the location of F11; C
363 represents the streamline at the location of F90; D represented the streamlines at the
364 location of F95.

365 While A streamlines are commonly observed in the *Homogeneous* scenario (Figure 4a),
366 they are absent in the layered scenarios. B streamlines in the *Layered: without faults*
367 scenario (Figure 4b) differ from those in the *Layered: low K fault* scenario (Figure 4c),
368 but they are similar to those in the *Layered: high K fault* scenario (Figure 4d), implying
369 impacts caused by the changes in permeability of the F11 fault core. In the *Layered:*

370 *low K fault* scenario, groundwater is hindered from flowing across the F11 fault zone
371 but is driven along the damage zone. However, the B streamlines in *Layered: high K*
372 *fault* indicate groundwater flowing across the F11 fault zone. The C and D streamlines
373 in the *Layered: low K fault* and *Layered: high K fault* scenarios show the same
374 distribution as F90 and F95 had identical permeabilities in these scenarios. In both
375 scenarios, C and D streamlines suggest impeded groundwater flow compared with that
376 in the *Layered: without faults* scenario.

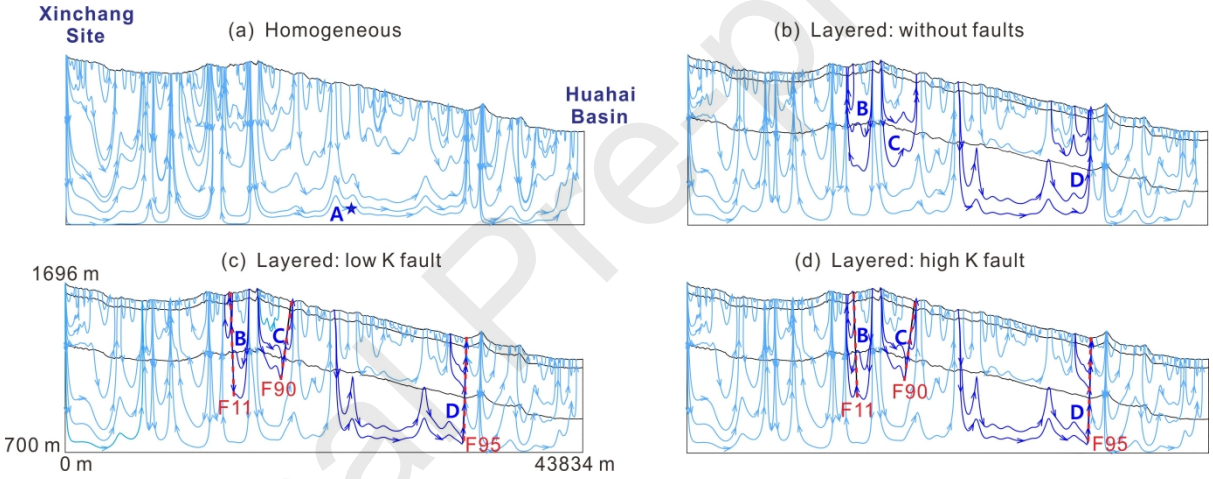

377

Figure 4. Streamline distributions of four model scenarios: A, B, and C represent observed streamlines to highlight the differences in groundwater flow patterns.

378 **5. Discussion**

379 *5.1 Depth trend of Bedrock K in crystalline basement*

380 The crystalline basement, being mostly granite and gneiss, is generally low-

conductivity media where interconnected fracture porosity and permeability determine groundwater flow behaviors (Rutqvist and Stephansson, 2003). The permeability of crystalline rocks varies in space both horizontally and vertically due to fracture interactions, and the vertical permeability is generally assumed to decrease with depth (Achtziger-Zupančič et al., 2017; Brace, 1980; Manning and Ingebritsen, 1999; Ranjram et al., 2015; Stober and Bucher, 2007). The decrease with depth was also observed in the *K* obtained in crystalline bedrock composed of gneiss and granite within 600 mbgs in this study (Fig 2a). High hydraulic conductivity values were mostly observed within depths of <100 m (especially within depths <50 m). The range between the maximum and minimum *K* decreased with depth from approximately 9 orders of magnitude (1E-14 to 1E -4 m·s-1) near the surface to approximately 4 orders of magnitude in the deepest interval (1E-12 to 1E -8 m·s-1) As lithology may be of less importance in crystalline rock permeability at near-surface depth (<1,000 m), the higher and more scattered *K* values near the surface may indicate greater sensitivity to weathering and tectonic setting alteration (Achtziger-Zupančič et al., 2017; Ranjram et al., 2015).

A total of 91% of Bedrock *K* is distributed between 1.03 E-12 $m \cdot s^{-1}$ – 9.82 E-8 $m \cdot s^{-1}$, which is generally less permeable than Carnmenellis Granite (Cornwall, UK) of similar depth (Watkins, 2007). As shown in Figure 5, the *K* range in the study area is of smaller

values and larger variance than that in the Black Forest area of Germany, which has a similar lithology of gneiss and granite (Stober and Bucher, 2007). The discrepancy is also obvious in the logarithmic fits for the depth trend of permeability. The resulting trend for Bedrock *K* in our study area yields a smaller slope and intercept than that derived in the Black Forest area by Stober and Bucher (2007), as well as the depth trend derived for a global database in crystalline rock by Achtziger- Zupančič et al. (2017). The slope and intercept are also substantially significantly lower than the widely cited curve derived by Manning and Ingebritsen (1999). This lack of agreement is expected as these fits are derived to describe permeability at larger depths than those reported in this study. Although Bedrock *K* in our study area verified the assumption of a decreased trend with depth, the low predictive power ($R^2 = 0.19$) demonstrated the invalidity of a consistent and generalizable equation capable of describing the K-z relationship in a crystalline basement. Similar results were reported for the analysis of crystalline rock datasets (Ranjram et al., 2015; Snowdon et al., 2021; Stober and Bucher, 2007).

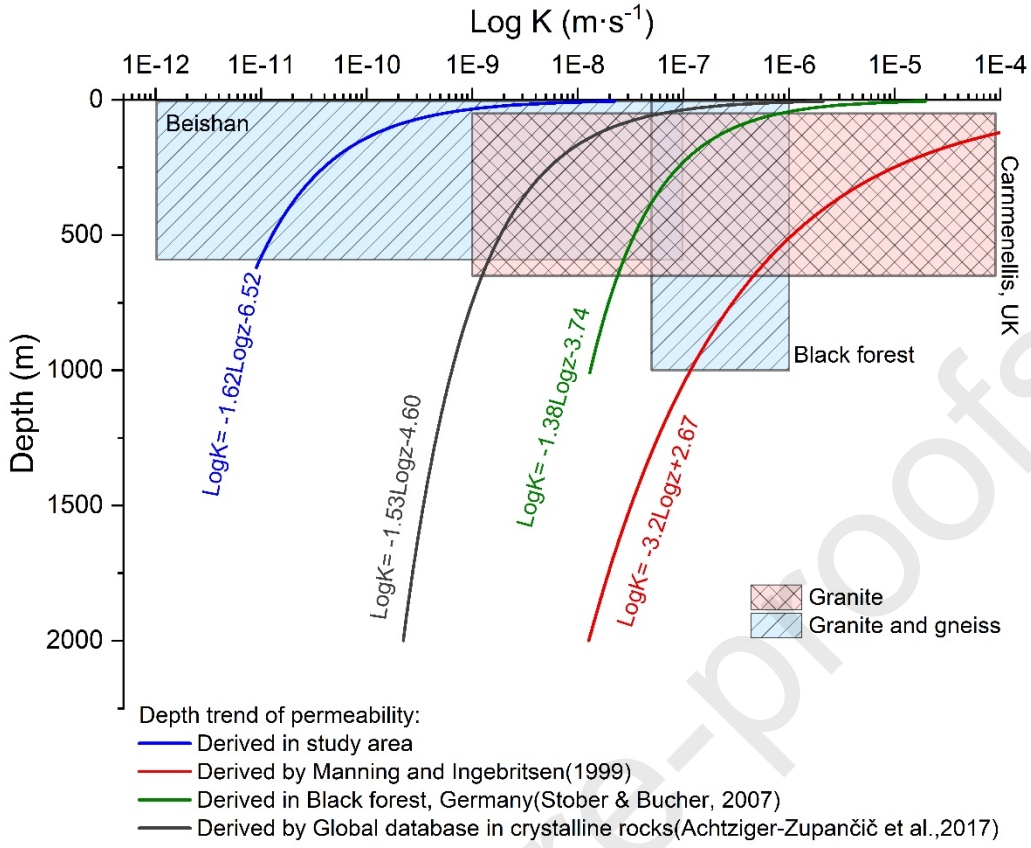

414

Figure 5. Comparison of hydraulic conductivity (K) ranges and the depth trends in crystalline bedrock.

415 *5.2 Permeability and flow behaviors in fault zones*

416 The permeability and flow behaviors in three faults (F11, F90, and F95) in this
417 mountain hydrogeological system are shown in Figures 3 and 4.

418 Fault zones created by brittle formation are composed of distinct components with
419 different permeability: fault cores and damage zones (Bense et al., 2013; Caine et al.,
420 1996; Rawling et al., 2001; Scibek, 2020). For a single fault, groundwater flows mainly

421 through connected open fractures in the damage zone; the proportion of damage zone
422 thickness to total fault thickness (F_a) enables the description of fault architecture and
423 flow behavior (Caine et al., 1996). With a F_a value close to 1 (0.98), the western part
424 (B-B') of F95 is likely to be of the "distributed conduit" type. However, the same fault
425 was identified to be a potential "barrier" according to the permeability ratio (Table 3)
426 and simulated streamlines from 2D numerical modelling. This suggested the complex
427 and combined role of F95 in this particular hydrogeological setting. With low
428 conductivity for the general fault zone, the groundwater was hindered from flowing
429 across the F95 towards the south in this two-dimensional model. Nevertheless, the
430 existence of a relatively more permeable damage zone with higher conductivity (5.35
431 E-7 $m \cdot s^{-1}$) in F95 suggests potential flow along the damage zone towards the southeast.

432 For F11, the discrepancy in fault core conductivity causes the spatial variability in
433 permeability structures, and thus affects the flow behavior in numerical modelling.
434 Groundwater flow was impeded from flowing across the F11 fault zone in the *Layered:*
435 *Low K fault* scenario (corresponding to the measurements on the western part A-A'),
436 acting as a barrier in MBR processes (Bresciani et al., 2018; Figueroa et al., 2021).
437 However, the flow was allowed to pass the same fault zone in the *Layered: High K fault*
438 scenario (corresponding to measurements on the western part B-B'), connecting
439 groundwater from both sides of fault zone (Roques et al., 2014). Consequently, the F11

fault zone partially impedes groundwater flow from flowing south, likely acting as a combined "conduit-barrier." Similar flow behavior and discontinuity in permeability of faults have been examined with numerical modelling (Mechal et al., 2016) and field investigation (Caine et al., 2017). The large discontinuity of the fault in the eastern Española Basin, Rio Grande rift, New Mexico, indicated that it was unlikely to systematically impede groundwater flow (Caine et al., 2017).

According to simulated streamline C in Figure 4, F90 is likely a barrier for groundwater flow in the study area. However, all three faults show only localized impact on streamline distribution, indicating the limitation of faults' effects on the hydrogeological process for this particular mountain bedrock groundwater system.

5.3 Possible MBR processes in the Beishan area

The streamline distributions in Figure 4 indicates no groundwater flow directly from the Xinchang Site to the Huahai Basin under the control of topography and generally low hydraulic conductivity in the Beishan area. Streamline A observed in the *Homogeneous* scenario was absent in all Layered scenarios, indicating the vertical heterogeneity of K might hinder groundwater from developing deeper circulation and therefore may prejudice diffuse MBR to the Hauhai Basin.

Although as an oblique-oriented fault, the F90 is likely to act as a hydraulic barrier to

458 diffuse MBR with available data. Groundwater flow towards the Huahai basin was
459 impeded from crossing the fault core zone of the obliquely oriented fault F95 in the 2D
460 section. However, the damage zone with relatively high conductivity and large
461 thickness may also function as a conduit driving groundwater flow within the connected
462 fractures, which is referred to as focused MBR. Consequently, the F95 is likely to act
463 as a combined "conduit-barrier", impeding diffuse MBR while permitting focused
464 MBR.

465 The spatial variability in permeability results in the difference in the hydraulic role of
466 F11. As C streamlines shown in Fig 4, the F11 was unlikely to systematically and
467 significantly impede diffuse MBR by allowing groundwater flow across its core in
468 partial sections. Therefore, the F11 may also act as a combined "conduit-barrier" for
469 MBR in the study area.

470 Despite its spatial discontinuity and small thickness in the study area, the canyons of
471 alluvial sediment could present a potential flow path for focused MBR (Markovich et
472 al., 2019), especially within the mountain front area near the Huahai Basin. This process
473 corresponds to the groundwater recharge through focused infiltration contributed by
474 ephemeral streams, which is associated with rainy events or snowmelt (Taucare et al.,
475 2020) and is highly sensitive to local weather. Indeed, the absence of snow and rare
476 rainy events in the study area suppress focused MBR through canyons.

6. Conclusion

This study examines the potential flow paths of MBR processes, mainly focusing on the vertical heterogeneity of *K* and the hydraulic role of fault zones in hydrogeological settings. We also provide a series of hydraulic conductivity data obtained by in-situ measurements from a crystalline mountain block system at various depths (0–592.34 m). We deciphered the flow paths originating from the Xinchang Site, Beishan area, and feeding adjacent aquifers in the Huahai Basin using a permeability conceptual model and numerical simulations of bedrock sections. These findings help to explain the MBR processes critical in determining the safety of a future HLW disposal site. The primary conclusions are as follows:

- Most Bedrock *K* (91%) is distributed between 1.03 E-12 $m \cdot s^{-1}$–9.82 E-8 $m \cdot s^{-1}$, which is generally lower than that in other sites with similar depth or lithology (Stober and Bucher, 2007; Watkins, 2007). Higher *K* values and larger variance were observed at shallow depths (<100 m, and especially <50 m), supporting the assumption that permeability is generally decreasing with depth. A logarithmic fit to Bedrock *K* (Log *K* = -1.62 Log z(m) - 6.72, R2 = 0.19) shows a smaller slope and intersect than those derived by Achtziger-Zupančič et al. (2017), Manning and

Ingebritsen (1999), and Stober and Bucher (2007). The discrepancy in data and trend line, as well as the low predictive power R^2, suggesting the ineffectiveness of a consistent and generalizable relationship between hydraulic conductivity and depth in a crystalline basement.

- No direct groundwater flow from the Xinchang Site to the Huahai Basin was observed according to the simulated streamlines. The vertical heterogeneity of *K* distribution restrained groundwater from deeper circulation, and may suppress diffuse MBR in the study area.
- Spatial variability of measured *K* in fault cores of fault F11 induces discontinuity in permeability, and therefore the difference in hydraulic roles to MBR. F11 is approximately perpendicular to the MBR flow direction, whereas it might act as a combined "conduit-barrier" according to the distribution of simulated streamlines in study area (Figure 4).
- With low conductivity of general fault zones, obliquely oriented faults F90 and F95 act as hydraulic barriers to diffuse MBR. However, the damage zone of relatively high conductivity could function as a conduit driving groundwater flow within connected fractures, promoting focused MBR of study area.

In summary, based on in-situ *K* data (n = 555), this study suggests the possible flow paths of MBR in a crystalline mountain block system, providing insights into the

514 characteristics of *K* in mountain bedrock. The study also provides insights into the
515 localized effects and spatially variable roles of fault zones in hydrogeological processes
516 within this particular hydrogeological configuration in Beishan, China. In addition, the
517 hydraulic conductivity data presented here can provide information on the subsurface
518 properties of mountain block systems in crystalline areas, and further facilitate the
519 characterization and quantification of mountain block recharge.

520 **CRediT authorship contribution statement**

521 **Yunmei Fu**: Conceptualization, Investigation, Methodology, Software, Formal
522 analysis, Visualization, Writing - original draft. **Yanhui Dong:** Funding acquisition,
523 Methodology, Project administration, Supervision, Writing - review and editing.
524 **Liheng Wang**: Investigation, Writing - review and editing. **Olivier Bour**: Visualization,
525 Writing - review and editing. **Maria V. Klepikova**: Visualization, Writing - review and
526 editing. **Zihua Zong**: Resources, Investigation. **Zhifang Xu**: Supervision, Writing -
527 review and editing. **Zichao Zhou**: Resources, Investigation.

528 **Declaration of Interest**

529 The authors declare that they have no known competing financial interests or personal
530 relationships that could have appeared to influence the work reported in this paper.

Acknowledgments

This work was financially supported by the Second Tibetan Plateau Scientific Expedition and Research Program (STEP) (Grant No.2019QZKK0904). We thank Beijing Research Institute of Uranium Geology for the in-situ test data. We also would like to thank Xingyun Liu for his perennial assistance in the field investigation. We thank all the people who were involved in the project: Ruiqi Duan, Luokun Xiao, Qian Zhang, Hong Zhang, Jingfan Ye, Ruili Ji, Ming Zhang, Hengrui Chen, etc. Finally, we greatly appreciate the dedicated revision made by the anonymous reviewers, which allowed us to thoroughly improve the quality of the article.

References

Achtziger-Zupančič, P., Loew, S., Mariéthoz, G., 2017. A new global database to improve predictions of permeability distribution in crystalline rocks at site scale. Journal of Geophysical Research: Solid Earth, 122(5): 3513-3539. DOI:https://doi.org/10.1002/2017JB014106

Aishlin, P., McNamara, J.P., 2011. Bedrock infiltration and mountain block recharge accounting using chloride mass balance. Hydrol. Process., 25(12): 1934-1948. DOI:https://doi.org/10.1002/hyp.7950

548 Ajami, H., Troch, P.A., Maddock III, T., Meixner, T., Eastoe, C., 2011. Quantifying
549 mountain block recharge by means of catchment-scale storage-discharge
550 relationships. Water Resour. Res., 47(4).
551 DOI:https://doi.org/10.1029/2010WR009598

552 Ameli, A.A., Gabrielli, C., Morgenstern, U., McDonnell, J.J., 2018. Groundwater
553 Subsidy From Headwaters to Their Parent Water Watershed: A Combined
554 Field-Modeling Approach. Water Resour. Res., 54(7): 5110-5125.
555 DOI:https://doi.org/10.1029/2017WR022356

556 Bense, V.F., Gleeson, T., Loveless, S.E., Bour, O., Scibek, J., 2013. Fault zone
557 hydrogeology. Earth-Sci. Rev., 127: 171-192.
558 DOI:10.1016/j.earscirev.2013.09.008

559 Bickle, M.J., 2009. Geological carbon storage. Nature Geoscience, 2(12): 815-818.
560 DOI:10.1038/ngeo687

561 Brace, W.F., 1980. Permeability of crystalline and argillaceous rocks. International
562 Journal of Rock Mechanics and Mining Sciences & Geomechanics Abstracts,
563 17(5): 241-251. DOI:https://doi.org/10.1016/0148-9062(80)90807-4

564 Bresciani, E. et al., 2018. Using hydraulic head, chloride and electrical conductivity

565 data to distinguish between mountain-front and mountain-block recharge to
566 basin aquifers. Hydrol. Earth Syst. Sci., 22(2): 1629-1648. DOI:10.5194/hess-
567 22-1629-2018

568 Caine, J.S., Evans, J.P., Forster, C.B., 1996. Fault zone architecture and permeability
569 structure. Geology, 24(11): 1025-1028. DOI:10.1130/0091-
570 7613(1996)024<1025:Fzaaps>2.3.Co;2

571 Caine, J.S., Minor, S.A., Grauch, V.J.S., Budahn, J.R., Keren, T.T., 2017. A
572 comprehensive survey of faults, breccias, and fractures in and flanking the
573 eastern Española Basin, Rio Grande rift, New Mexico. Geosphere, 13(5): 1566-
574 1609. DOI:10.1130/ges01348.1

575 Cao, X.Y., Hu, L.T., Wang, J.S., Wang, J.R., 2017a. Radionuclide transport model for
576 risk evaluation of high-level radioactive waste in Northwestern China. Hum.
577 Ecol. Risk Assess., 23(8): 2017-2032. DOI:10.1080/10807039.2017.1361811

578 Cao, X.Y., Hu, L.T., Wang, J.S., Wang, J.R., 2017b. Regional Groundwater Flow
579 Assessment in a Prospective High-Level Radioactive Waste Repository of
580 China. Water, 9(7): 15. DOI:10.3390/w9070551

581 Chowdhury, A.H., Uliana, M., Wade, S., 2008. Ground Water Recharge and Flow

582 Characterization Using Multiple Isotopes. Groundwater, 46(3): 426-436.
583 DOI:https://doi.org/10.1111/j.1745-6584.2008.00443.x

584 Delinom, R.M., 2009. Structural geology controls on groundwater flow: Lembang Fault
585 case study, West Java, Indonesia. Hydrogeol. J., 17(4): 1011-1023.
586 DOI:10.1007/s10040-009-0453-z

587 Dong, Y.H., Li, G.M., Li, M., 2009. Numerical modeling of the regional ground water
588 flow in Beishan area, Gansu Province. Chin. Sci. Bull., 54(17): 3112-3115.
589 DOI:10.1007/s11434-009-0344-7

590 Engdahl, N.B., Maxwell, R.M., 2015. Quantifying changes in age distributions and the
591 hydrologic balance of a high-mountain watershed from climate induced
592 variations in recharge. J. Hydrol., 522: 152-162.
593 DOI:https://doi.org/10.1016/j.jhydrol.2014.12.032

594 Figueroa, R. et al., 2021. Deciphering groundwater flow-paths in fault-controlled
595 semiarid mountain front zones (Central Chile). Science of The Total
596 Environment, 771: 145456.
597 DOI:https://doi.org/10.1016/j.scitotenv.2021.145456

598 Forster, C., Smith, L., 1988. Groundwater flow systems in mountainous terrain: 2.

599 Controlling factors. Water Resour. Res., 24(7): 1011-1023.
600 DOI:https://doi.org/10.1029/WR024i007p01011

601 Gansu Geology Survey, 1978. The report and map for hydrogeological survey in the
602 Jiujing and Yumen (1: 200,000), Gansu Science and Technology Press,
603 Lanzhou.

604 Gleeson, T., Manning, A.H., 2008. Regional groundwater flow in mountainous terrain:
605 Three-dimensional simulations of topographic and hydrogeologic controls.
606 Water Resour. Res., 44(10): 16. DOI:10.1029/2008wr006848

607 Gunter, W.D., Bachu, S., Benson, S., 2004. The role of hydrogeological and
608 geochemical trapping in sedimentary basins for secure geological storage of
609 carbon dioxide. Geological Society, London, Special Publications, 233(1): 129-
610 145. DOI:10.1144/gsl.Sp.2004.233.01.09

611 Guo, Y., Liu, S., Lu, C., 2003. Isotope Characteristics of Groundwater in the Potential
612 Site of a High-level Waste Repository in China (in Chinese). Acta Geoscientica
613 Sinica(06): 525-528.

614 Guo, Y. et al., 2014. Synthetic hydrogeological study on Beishan preselected area for
615 high-level radioactive waste repository in China (in Chinese). World Nuclear

616 Geoscience, 31(04): 587-593.

617 Haitjema, H.M., Mitchell-Bruker, S., 2005. Are Water Tables a Subdued Replica of the
618 Topography? Groundwater, 43(6): 781-786.
619 DOI:https://doi.org/10.1111/j.1745-6584.2005.00090.x

620 Healy, R.W., 2010. Estimating groundwater recharge. Cambridge university press.

621 Jódar, J. et al., 2017. Groundwater discharge in high-mountain watersheds: A valuable
622 resource for downstream semi-arid zones. The case of the Bérchules River in
623 Sierra Nevada (Southern Spain). Science of The Total Environment, 593-594:
624 760-772. DOI:https://doi.org/10.1016/j.scitotenv.2017.03.190

625 Kebede, S. et al., 2008. Groundwater origin and flow along selected transects in
626 Ethiopian rift volcanic aquifers. Hydrogeol. J., 16(1): 55. DOI:10.1007/s10040-
627 007-0210-0

628 Li, Y., 2020. Groundwater hydrochemical characteristics and water-rock interaction in
629 Beishan area, Gansu (in Chinese). Doctoral Thesis, Beijing Research Institute
630 of Uranium Geology.

631 Lone, S.A. et al., 2021. Meltwaters dominate groundwater recharge in cold arid desert
632 of Upper Indus River Basin (UIRB), western Himalayas. Science of The Total

633 Environment, 786: 147514.
634 DOI:https://doi.org/10.1016/j.scitotenv.2021.147514

635 Manning, A.H., Caine, J.S., 2007. Groundwater noble gas, age, and temperature
636 signatures in an Alpine watershed: Valuable tools in conceptual model
637 development. Water Resour. Res., 43(4).
638 DOI:https://doi.org/10.1029/2006WR005349

639 Manning, A.H., Solomon, D.K., 2003. Using noble gases to investigate mountain-front
640 recharge. J. Hydrol., 275(3): 194-207. DOI:https://doi.org/10.1016/S0022-
641 1694(03)00043-X

642 Manning, C.E., Ingebritsen, S.E., 1999. Permeability of the continental crust:
643 Implications of geothermal data and metamorphic systems. Rev. Geophys.,
644 37(1): 127-150. DOI:10.1029/1998rg900002

645 Markovich, K.H., Manning, A.H., Condon, L.E., McIntosh, J., 2019. Mountain-block
646 recharge: A review of current understanding. Water Resour. Res., 55(11): 8278-
647 8304. DOI:10.1029/2019wr025676

648 Mechal, A., Birk, S., Winkler, G., Wagner, T., Mogessie, A., 2016. Characterizing
649 regional groundwater flow in the Ethiopian Rift: A multimodel approach

650 applied to Gidabo River Basin. Austrian Journal of Earth Sciences, 109(1).

651 Peng, N., 2013. Basin analysis and paleogeography in northe Qilian Mountain to
652 Beishan area, early Cretaceous (in Chinese). Doctoral Thesis, China University
653 of Geosciences (Beijing).

654 Peng, T.-R. et al., 2018. Assessing the recharge process and importance of montane
655 water to adjacent tectonic valley-plain groundwater using a ternary end-member
656 mixing analysis based on isotopic and chemical tracers. Hydrogeol. J., 26(6):
657 2041-2055. DOI:10.1007/s10040-018-1741-2

658 Ranjram, M., Gleeson, T., Luijendijk, E., 2015. Is the permeability of crystalline rock
659 in the shallow crust related to depth, lithology or tectonic setting? Geofluids,
660 15(1-2): 106-119. DOI:https://doi.org/10.1111/gfl.12098

661 Rapp, G.A., Condon, L.E., Markovich, K.H., 2020. Sensitivity of simulated mountain
662 block hydrology to subsurface conceptualization. Water Resour. Res., 56(10):
663 21. DOI:10.1029/2020wr027714

664 Rawling, G.C., Goodwin, L.B., Wilson, J.L., 2001. Internal architecture, permeability
665 structure, and hydrologic significance of contrasting fault-zone types. Geology,
666 29(1): 43-46. DOI:10.1130/0091-7613(2001)029<0043:Iapsah>2.0.Co;2

667 Roques, C. et al., 2014. Hydrological behavior of a deep sub-vertical fault in crystalline
668 basement and relationships with surrounding reservoirs. J. Hydrol., 509: 42-54.
669 DOI:https://doi.org/10.1016/j.jhydrol.2013.11.023

670 Rutqvist, J., Stephansson, O., 2003. The role of hydromechanical coupling in fractured
671 rock engineering. Hydrogeol. J., 11(1): 7-40.

672 Scibek, J., 2020. Multidisciplinary database of permeability of fault zones and
673 surrounding protolith rocks at world-wide sites. Sci. Data, 7(1): 95.
674 DOI:10.1038/s41597-020-0435-5

675 Scibek, J., Gleeson, T., McKenzie, J.M., 2016. The biases and trends in fault zone
676 hydrogeology conceptual models: global compilation and categorical data
677 analysis. Geofluids, 16(4): 782-798. DOI:https://doi.org/10.1111/gfl.12188

678 Snowdon, A.P., Normani, S.D., Sykes, J.F., 2021. Analysis of Crystalline Rock
679 Permeability Versus Depth in a Canadian Precambrian Rock Setting. Journal of
680 Geophysical Research: Solid Earth, 126(5): e2020JB020998.
681 DOI:https://doi.org/10.1029/2020JB020998

682 Somers, L.D., McKenzie, J.M., 2020. A review of groundwater in high mountain
683 environments. WIREs Water, 7(6): e1475.

684 DOI:https://doi.org/10.1002/wat2.1475

685 Stober, I., Bucher, K., 2007. Hydraulic properties of the crystalline basement.
686 Hydrogeol. J., 15(2): 213-224. DOI:10.1007/s10040-006-0094-4

687 Taucare, M., Daniele, L., Viguier, B., Vallejos, A., Arancibia, G., 2020. Groundwater
688 resources and recharge processes in the Western Andean Front of Central Chile.
689 Science of The Total Environment, 722: 137824.
690 DOI:https://doi.org/10.1016/j.scitotenv.2020.137824

691 Tóth, J., Sheng, G., 1996. Enhancing safety of nuclear waste disposal by exploiting
692 regional groundwater flow: The recharge area concept. Hydrogeol. J., 4(4): 4-
693 25.

694 Viviroli, D., Kummu, M., Meybeck, M., Kallio, M., Wada, Y., 2020. Increasing
695 dependence of lowland populations on mountain water resources. Nature
696 Sustainability, 3(11): 917-928. DOI:10.1038/s41893-020-0559-9

697 Voeckler, H.M., Allen, D.M., Alila, Y., 2014. Modeling coupled surface water –
698 Groundwater processes in a small mountainous headwater catchment. J. Hydrol.,
699 517: 1089-1106. DOI:https://doi.org/10.1016/j.jhydrol.2014.06.015

700 Voss, C., Provost, A., 2001. Recharge-area nuclear waste repository in Southeastern

701 Sweden. Demonstration of hydrogeologic siting concepts and techniques. SKI
702 Report, 1: 44.

703 Wang, C., Gomez-Velez, J.D., Wilson, J.L., 2018a. The importance of capturing
704 topographic features for modeling groundwater flow and transport in
705 mountainous watersheds. Water Resour. Res., 54(12): 10,313-10,338.
706 DOI:https://doi.org/10.1029/2018WR023863

707 Wang, J., Chen, L., Su, R., Zhao, X.G., 2018b. The Beishan underground research
708 laboratory for geological disposal of high-level radioactive waste in China:
709 Planning, site selection, site characterization and in situ tests. J. Rock Mech.
710 Geotech. Eng., 10(3): 411-435. DOI:10.1016/j.jrmge.2018.03.002

711 Wang, L., 2015. Multi-scale groundwater numerical simulation study of regional-basin-
712 site in Gansu Beishan Area (in Chinese). Doctoral Thesis, University of Chinese
713 Academy of Sciences, Beijing.

714 Watkins, D.C., 2007. Determining a representative hydraulic conductivity of the
715 Carnmenellis Granite of Cornwall, UK, based on a range of sources of
716 information. Groundwater in fractured rocks. International Association of
717 Hydrogeologists Selected Papers, 9: 151-162.

718 Welch, L.A., Allen, D.M., 2014. Hydraulic conductivity characteristics in mountains
719 and implications for conceptualizing bedrock groundwater flow. Hydrogeol. J.,
720 22(5): 1003-1026. DOI:10.1007/s10040-014-1121-5

721 Welch, L.A., Allen, D.M., van Meerveld, H.J., 2012. Topographic Controls on Deep
722 Groundwater Contributions to Mountain Headwater Streams and Sensitivity to
723 Available Recharge. Can. Water Resour. J., 37(4): 349-371.
724 DOI:10.4296/cwrj2011-907

725 Wilson, J.L., Guan, H.D., 2004. Mountain-block hydrology and mountain-front
726 recharge. Groundwater Recharge in a Desert Environment: The Southwestern
727 United States, 9: 113-137.

728 Yao, Y.Y. et al., 2017. What controls the partitioning between baseflow and mountain
729 block recharge in the Qinghai-Tibet Plateau? Geophys. Res. Lett., 44(16): 8352-
730 8358. DOI:10.1002/2017gl074344

731 Zhao, X.G. et al., 2016. Experimental investigations on the thermal conductivity
732 characteristics of Beishan granitic rocks for China's HLW disposal.
733 Tectonophysics, 683: 124-137.
734 DOI:https://doi.org/10.1016/j.tecto.2016.06.021

735 Zhou, Z. et al., 2020. Hydrogeochemical and isotopic characteristics of groundwater in
736 Xinchang preselected site and their implications. Environmental Science and
737 Pollution Research, 27(28): 34734-34745. DOI:10.1007/s11356-019-07208-1

738 **Abstract**

739 The process wherein groundwater flowing from mountain bedrock into lowland and
740 adjacent alluvial aquifers, known as mountain-block recharge (MBR), is found across
741 various climatic and geological settings. An understanding of the potential groundwater
742 flow paths in mountain block systems is necessary for comprehending MBR spatial
743 distribution. However, poorly characterized mountain block hydraulic properties, and
744 especially a lack of direct measurements of hydraulic conductivity (*K*) at depths >200
745 m, limit the characterization and quantifications of the MBR processes. In this study,
746 we analyze hydraulic data set, namely 555 in-situ *K* measurements at various depths
747 from two borehole sections extending from mountain block to mountain front in a
748 potential disposal site for high-level radioactive waste. The *K* dataset was categorized
749 into two groups: one for bedrock and another for fault zones, which was further
750 classified into fault core *K*, damage zone *K*, and general fault zone *K*. Using a
751 permeability conceptual model and multiple scenarios numerical modelling, this study
752 examined the potential flow paths of MBR processes, mainly focusing on the
753 characteristics of *K* in bedrocks and the hydraulic role of fault zones in mountain block

754 systems. The distribution of Bedrock *K* supports the assumption of decreased trend with
755 depth. A logarithmic fit through Bedrock *K* and depth pairs resulted in Log(K) = -
756 1.62*Log(z) - 6.52, with low predictive power. This study illustrated the localized
757 effects and spatially variable roles of fault zones in MBR within this particular
758 hydrogeological configuration in Beishan, China. Our results provide insights into the
759 MBR process in crystalline mountain block systems. Additionally, the hydraulic
760 conductivity presented here provides data on the subsurface properties of mountain
761 block systems in a crystalline area, and further facilitates the characterization and
762 quantification of mountain-block recharge.

763 **Keywords:** mountain block recharge, mountain hydrogeology, fractured aquifer

764

765 **Declaration of interests**
766
767 ☒ The authors declare that they have no known competing financial interests or personal
768 relationships that could have appeared to influence the work reported in this paper.
769
770 ☐ The authors declare the following financial interests/personal relationships which may be
771 considered as potential competing interests:
772
773
774
775
776
777

778

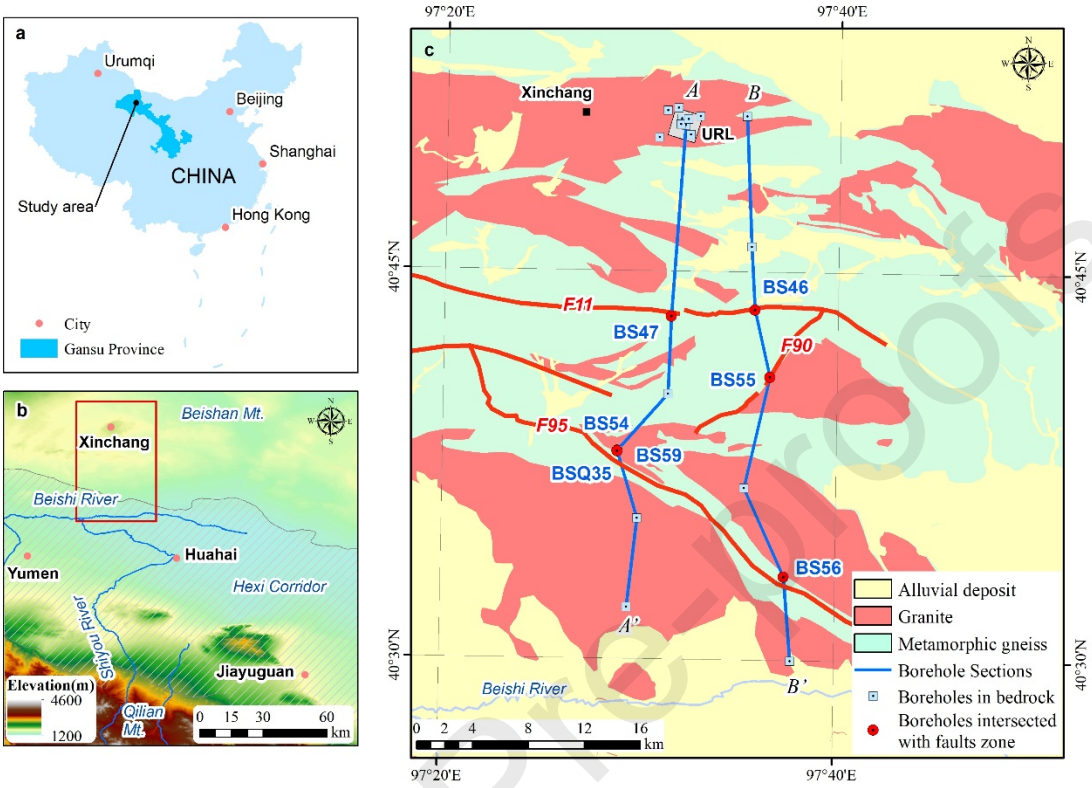

779

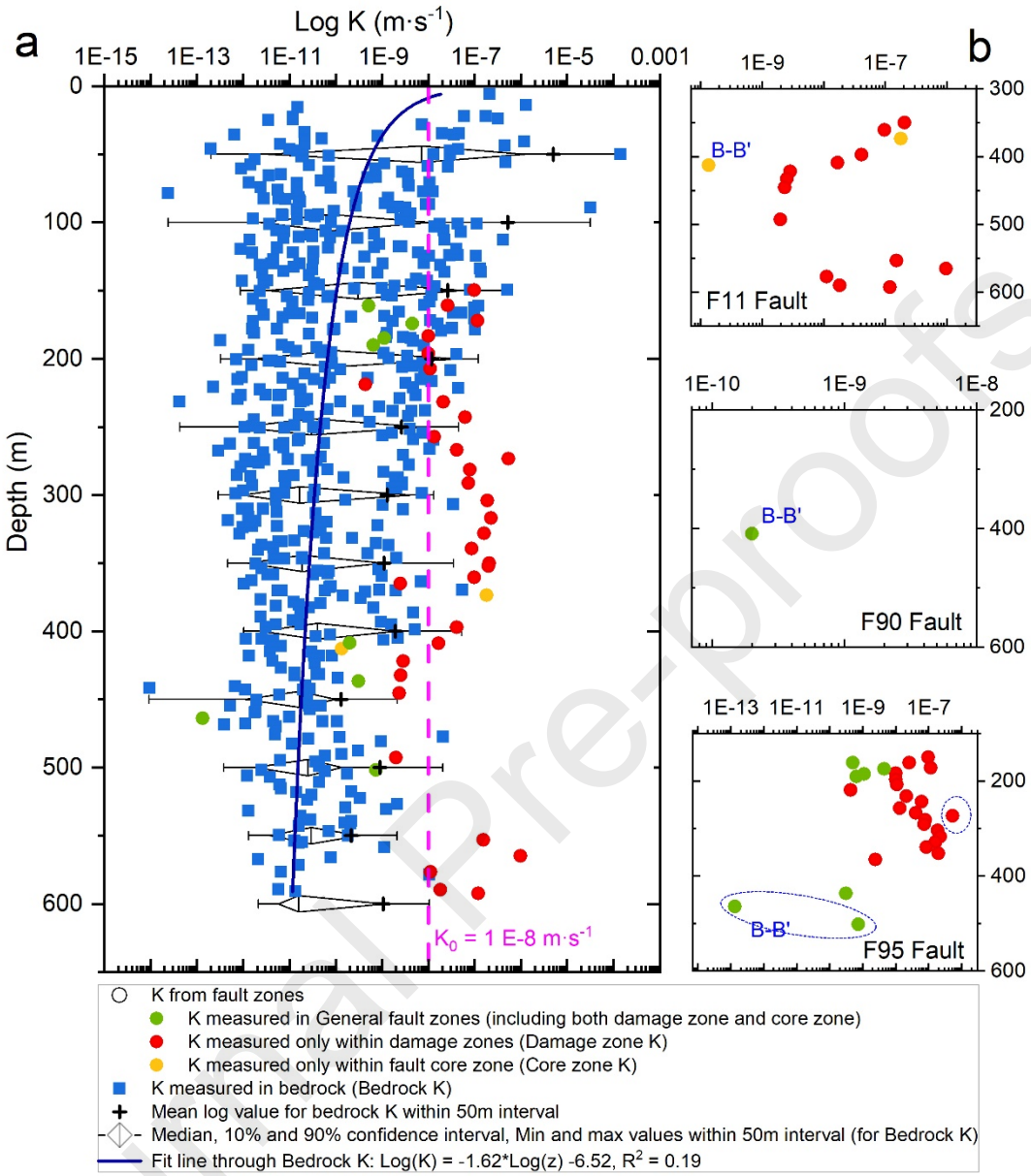

780

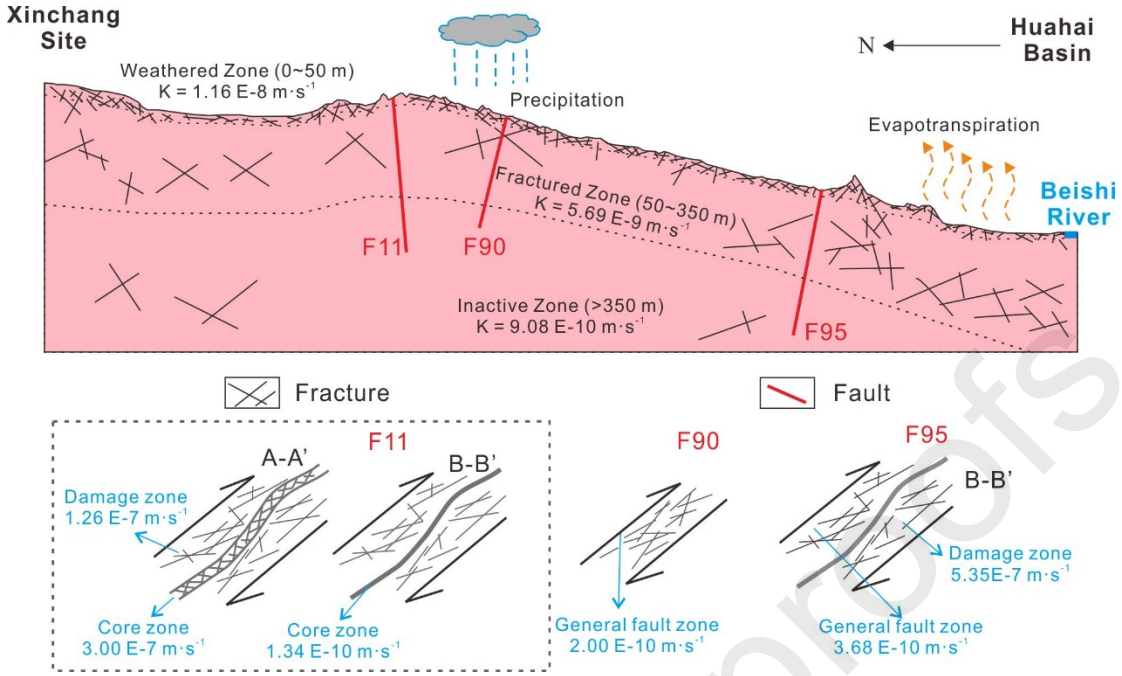

781

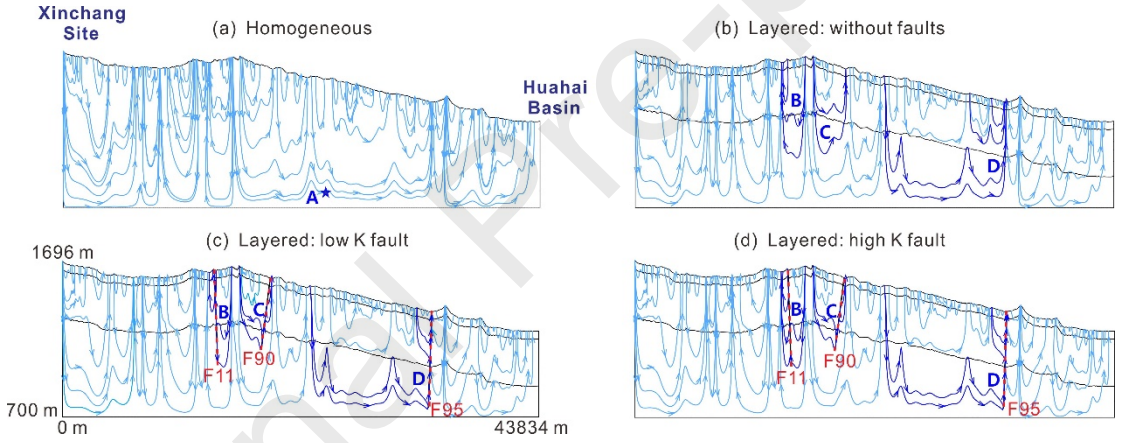

782

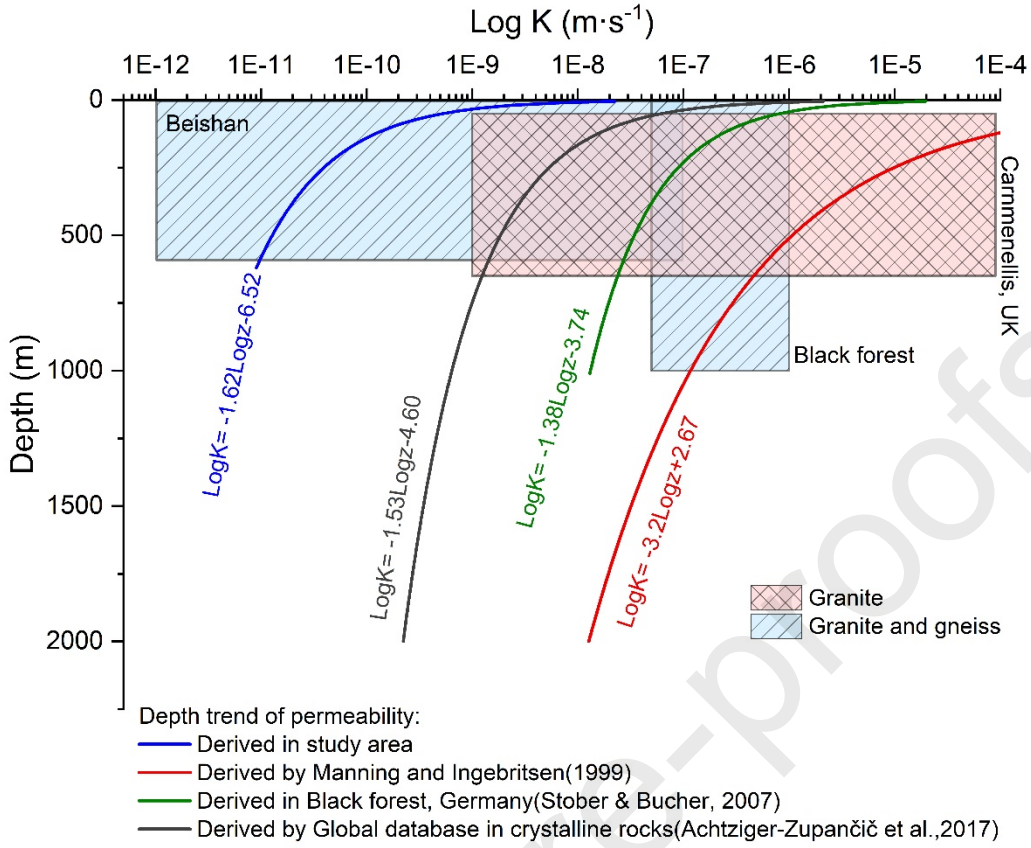

783

784 **Highlights**

785 ● Potential flow paths of MBR process in crystalline mountain block systems

786 were explored based on hydraulic conductivity data up to ~592.34 m depth.

787 ● Characteristics of hydraulic conductivity for bedrock and fault zones including

788 core zones and damage zones were reported.

789 ● Spatial discontinuities in the permeability may exist for the same fault, which

790 lead to its role can be either a conduit or a barrier in the MBR process.

791